

Electronic Supporting Information

Detecting Structural Transformation of Cobalt Phosphonate to Active Bifunctional Catalysts for Electrochemical Water-Splitting

Arindam Indra,^{a,b} Prashanth W. Menezes,^{b,*} Ivelina Zaharieva,^c Holger Dau,^{c,*} and Matthias Driess^{b,*}

^aDepartment of Chemistry, Indian Institute of Technology (BHU), Varanasi, Uttar Pradesh-221005, India

^bDepartment of Chemistry: Metalorganics and Inorganic Materials, Technische Universität Berlin, Straße des 17 Juni 135, Sekr. C2, 10623 Berlin, Germany

^cFachbereich Physik, Freie Universität Berlin, Arnimallee 14, 14195 Berlin, Germany

Experimental Section

Chemicals

All the chemicals are purchased from either Sigma Aldrich or Alfa-Aesar and used without further purification.

Instruments

Powder XRD measurements were carried out in Bruker AXS D8 advanced diffractometer equipped with a position sensitive detector (PSD) and curved germanium (111) primary monochromator. The radiation used was Cu- $K\alpha$ ($\lambda = 1.5418 \text{ \AA}$).

SEM studies have been performed in a Hitachi S-2700 microscope. TEM images were acquired in FEI Tecnai G² 20 S-TWIN transmission electron microscope (FEI Company, Eindhoven, Netherlands) equipped with a LaB₆-source at 200 kV acceleration voltage. EDX-analysis were performed with an EDAX r-TEM SUTW Detector (Si (Li)-detector). Both SEM and TEM measurements were performed at the Zentrum für Elektronenmikroskopie (ZELMI) of Technische Universität Berlin.

The XPS measurements were performed in a Kratos Axis Ultra X-ray photoelectron spectrometer (Kratos Analytical Ltd., Manchester, UK) by using Al $K\alpha$ monochromatic radiation source (1486.7 eV) with 90° take-off angle. The XPS spectra were collected with pass energy 20 eV and step 0.1 eV. The binding energies have been calibrated against C1s peak at 285.0 eV. Data analyses were carried out by using Casa XPS (Casa Software Ltd.).

The surface area and the pore size distributions were determined by using Quantachrome Autosorb-1 apparatus. Nitrogen adsorption/desorption isotherms were recorded at -196 °C after degassing the sample at 150 °C overnight. The BET surface area (S_{BET}) was estimated by

adsorption data in a relative pressure range from 0.01 to 0.1 and the pore size distribution was determined by analyzing the adsorption data of the N₂ isotherm using the Barret-Joyner-Halenda (BJH) method.

The elemental analysis was carried out on a Thermo Finnigan Flash EA 1112 Series instrument. The sample was prepared in silver-capsule for measuring accurate measurements. The samples were measured thrice and the average data was presented. Calibration of the instrument was carried out with the sample from the supplier of the instrument.

The composition of the materials after the electrochemistry was determined by ICP-AES on a Thermo Jarrell Ash Trace Scan analyzer. The films were dissolved in acid solutions and the three independent measurements were averaged.

X-ray absorption spectroscopy (XAS)¹

The *quasi in-situ* X-ray absorption spectra (XANES/EXAFS) were collected at the BESSY synchrotron radiation source operated by the Helmholtz-Zentrum Berlin. The measurements were conducted at the KMC-3 bending-magnet beamline at 20 K in a helium-flow cryostat (Oxford-Danfysik). The incident beam energy was selected by a Si(111) double-crystal monochromator. The measurements at the cobalt *K*-edge were performed in transmission mode with an ionization chamber and fluorescence mode using 13-element energy-resolving Ge detector (Canberra). The extracted spectrum was weighted by k^3 and simulated in k -space ($E_0 = 7710$ eV). All EXAFS simulations were performed using in-house software (SimX) after calculation of the phase functions with the FEFF program (version 8.4, self-consistent field option activated).² The data range used in the simulation of the EXAFS spectra was 25–1000 eV (3–16 Å⁻¹). The EXAFS simulation was optimized by a minimization of the error sum obtained by the summation of the squared deviations between measured and simulated values (least-squares fit). The fit was performed using the Levenberg-Marquardt method with numerical derivatives. The error ranges of the fit parameters were estimated from the covariance matrix of the fit. Further details are given elsewhere.³

CoPn samples for XAS experiments were prepared on fluorinated tin oxide substrates in analogy to the electrochemical experiments. The samples were electrochemically treated for OER CV (3 cycles), HER CV (3 cycles) and OER CA (25 h) at 1.56 V vs RHE and HER CA (25 h) at -0.36 V vs RHE (maintaining the current density of 10 and -10 mA cm⁻²) in 1 M aqueous KOH solutions. After the desired electrochemical measurement, the samples were immediately freeze-quenched using liquid N₂ under vigorous Ar gas flow and stored in liquid N₂ until XAS measurements were conducted.

Syntheses of the CoPn catalyst

3 mmol Co(NO₃)₂·6H₂O was dissolved in 10 mL water and mixed with 1:1 ethanol:H₂O solution (20 mL) of diethylenetriamine penta(methylenephosphonic acid) [DTPMP, 0.4 mmol] and stirred for 30 min. The pH of the solution was maintained to 5 by using ammonia and HCl. The mixture was stirred for another 6 h at room temperature and transferred into a 50 mL Teflon coated autoclave and heated for 24 h at 160 °C. The solid was collected after cooling down the autoclave and washed several times with water/ethanol and dried at 60 °C to get the violet-colored solid.

Synthesis of CoOOH

The commercially available $\text{Co}(\text{OH})_2$ was dispersed in 30 mL 4 M KOH solution which was then heated slowly up to 45 °C. 2 mL of 30% H_2O_2 solution was then added dropwise and was kept at the same temperature for 18 h. The final brown precipitate was filtered and washed with deionized water three times, then dried at 65 °C overnight in air.

Electrochemical measurements

The electrodes were prepared by electrophoretic deposition (EPD) method by applying a potential difference of 10 V between anode and cathode in a solution of iodine (for 50 mg of catalyst, 3 mg of iodine) and acetone (10 mL) on 1x1 cm² area of fluorinated tin oxide coated glass (FTO, Sigma Aldrich, resistivity 8-12 $\Omega/\text{sq.}$). The EPD was carried out for 3 minutes for each electrode. Similarly, the deposition of the materials on nickel foam (NF, Racemate BV) was also performed by the EPD method. The catalytic activity of the materials was measured in 1 M aqueous KOH solution at room temperature using a single-compartment three-electrode cell (material deposited on FTO-glass as a working electrode, Pt wire (or graphite rod) as a counter electrode and Hg/HgO reference electrode). The electrochemical measurements were performed by employing a potentiostat (SP-200, BioLogic Science Instruments) controlled by EC-Lab v10.20 software package.

Cyclic voltammetry (CV) and linear sweep voltammetry (LSV) were measured with 85% iR compensation. The potentials presented in this work were referenced to the reversible hydrogen electrode (RHE) through RHE calibration, $E(\text{RHE}) = E(\text{Hg}/\text{HgO}) + 0.098 \text{ V} + (0.059 \times \text{pH}) \text{ V}$. Chronoamperometric measurements were carried out in 1 M KOH at constant potentials (at a current density of 10 mA cm⁻²) vs. RHE.

The overall water splitting reaction was performed in a two-electrode system with CoPn deposited on NF as anode and cathode. The long-term stability under chronoamperometric conditions was also performed for 68 h at a selected potential when the current density reached 10 mA cm⁻².

The electrochemically active surface area (ECSA) of the catalyst was attained by determining electrochemical double-layer capacitance, C_{dl} , which was calculated from CV curves recorded in a potential range with no Faradaic current at different scan rates from 10 to 200 mV s⁻¹ (cycled between 0.92 and 0.97 V vs. RHE).⁴ The anodic charging currents measured were plotted as a function of the scan rate and from the slope, C_{dl} was obtained. The ECSA of a catalyst was then calculated using $\text{ECSA} = C_{\text{dl}}/C_s$ where C_s is the specific capacitance of the material per unit area under identical electrolyte conditions. For our estimation, we have used a specific capacitance C_s of 1.7 mF cm⁻² based on the literature reported values of NF in 1 M aqueous KOH solution.⁵

Electrochemical impedance spectroscopy (EIS) was performed at 1.55 V vs. RHE to obtain the Nyquist plots. The amplitude of the sinusoidal wave was examined in a frequency range of 100 kHz to 1 MHz. The impedance spectra were fitted using an equivalent RC circuit model. The charge-transfer resistance (R_{ct}) was then determined from the diameter of the semicircle in the Nyquist plots.

Figures

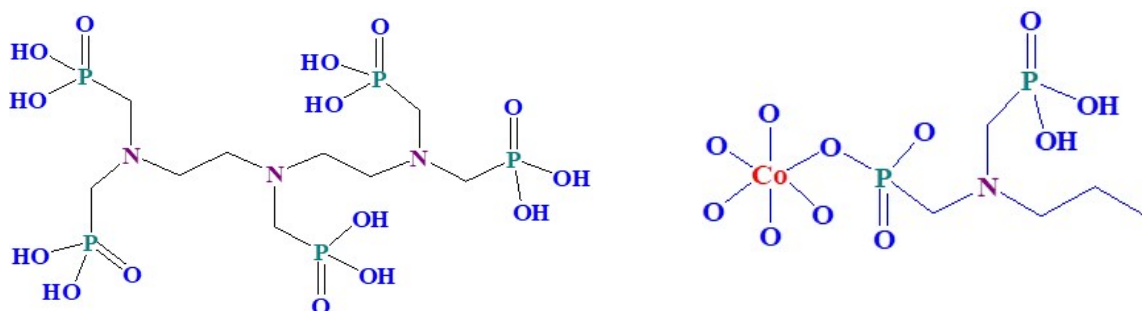


Figure S1. (Left) Structure of diethylenetriamine penta(methylenephosphonic acid) and (right) binding mode of PO_x unit with Co^{II} ion. The formula of the compound is determined to be Co_{7.5}(C₉H₂₈N₃O₁₅P₅)·xH₂O where Co^{II} ions are octahedrally surrounded by six oxygen atoms to form the CoO₆ unit. After the electrochemical transformation at the anode and cathode, the local environment around the cobalt center is changed to form new active catalysts (see later).

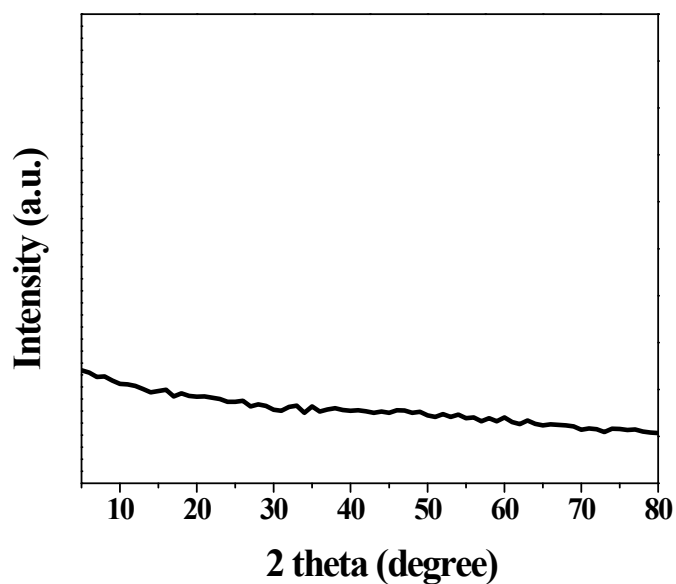


Figure S2. PXRD pattern showing the amorphous nature of the freshly prepared cobalt phosphonate (CoPn).

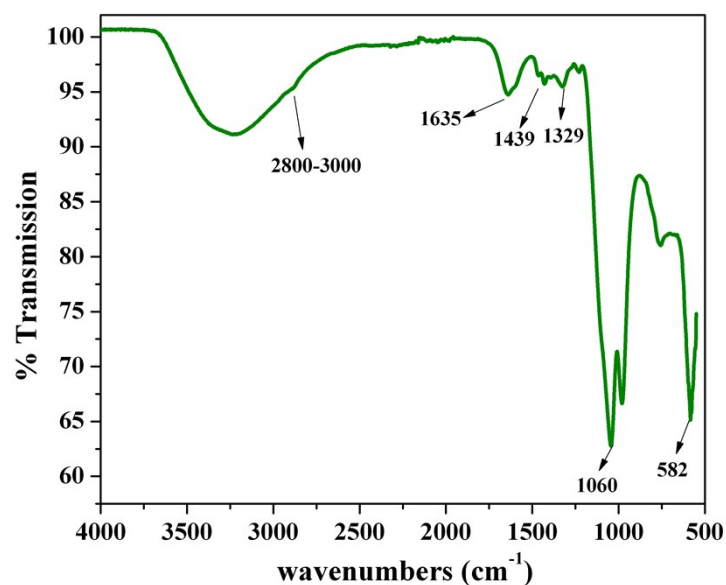


Figure S3. FT-IR spectra of CoPn. The band at 582 cm^{-1} is correlated to the stretching vibrations of Co-O bond whereas a sharp band at 1060 cm^{-1} can be attributed to the P-O-Co vibrations indicating the condensation of organic-inorganic species with the phosphonate structure.⁶ In addition to this, the band at 1329 cm^{-1} is associated with C-N stretching and the shoulder at 1439 cm^{-1} is related to the P-C vibrations.⁶ Further, the small peak at around 2800 to 3000 cm^{-1} corresponds to the C-H stretching modes of methylene carbon atoms in the organophosphonic linkages. Finally, the broad bands at ~ 3400 and 1635 cm^{-1} are from the adsorbed water and hydroxyl group.⁶

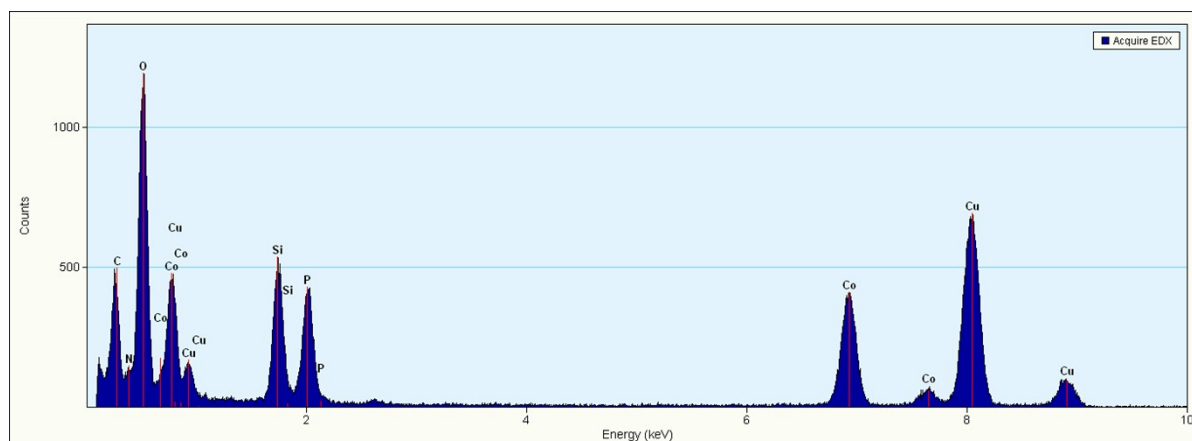


Figure S4. EDX spectrum of CoPn showing the presence of corresponding elements. The signal of Cu is from the grid of the TEM holder.

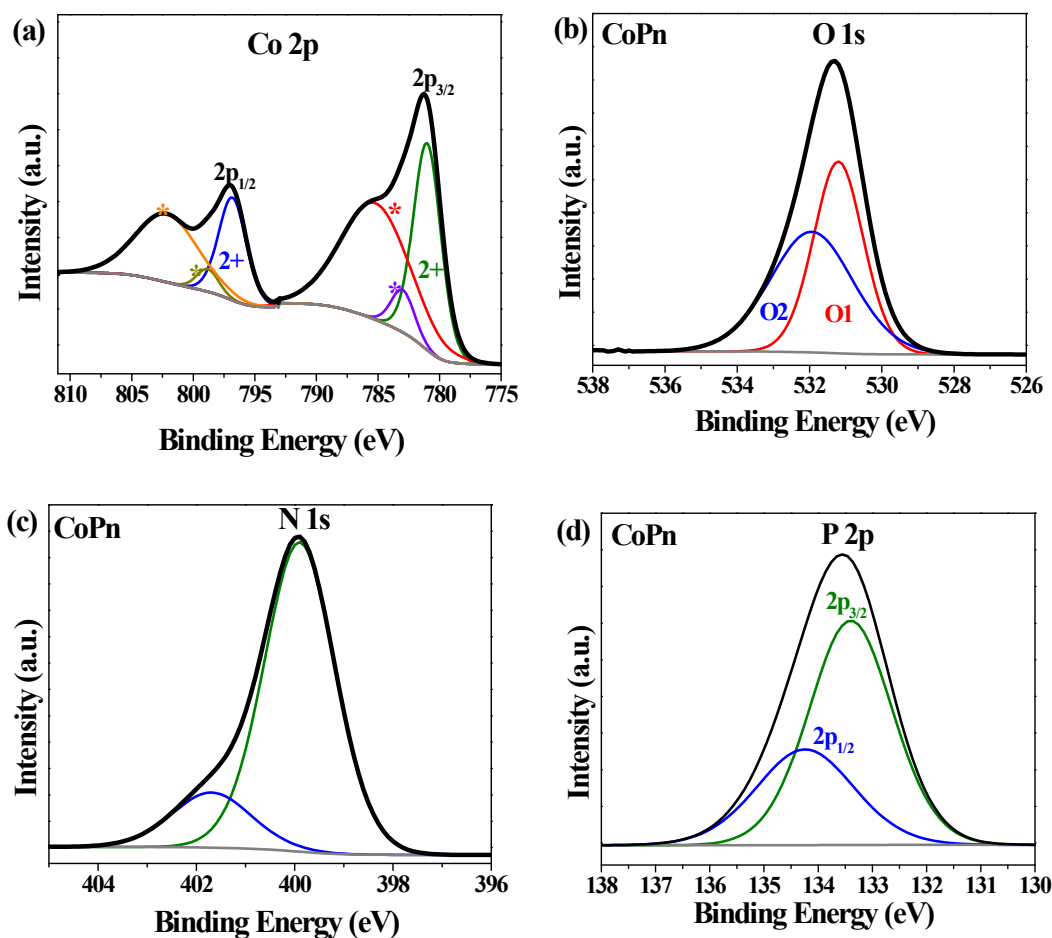


Figure S5. (a) Co 2p XPS studies indicate the presence of Co^{2+} as the major component in fresh CoPn. The $2p_{3/2}$ - $2p_{1/2}$ spin-orbit coupling spacing of 15.96 eV further confirms the presence of Co^{2+} as the dominant species. The origin of strong satellite peaks (*) also demonstrates the presence of Co^{2+} .⁷ (b) O 1s XPS studies for the fresh CoPn. O 1s spectrum was deconvoluted into two peaks: O1 at ~ 531.2 eV corresponding to P-O-Co moiety and O2 at ~ 532.0 eV representing the oxygen from water.⁷ (c) N 1s XPS studies for the fresh CoPn. The N 1s spectrum of fresh CoPn was deconvoluted into two peaks at 399.9 eV and 401.8 eV representing the C-N-containing moiety and quaternary N.⁶ and (d) P 2p XPS studies for the fresh CoPn. The peaks at binding energy ~ 133.4 eV and 134.3 eV clearly indicated the presence of PO_x unit in phosphonate.⁶

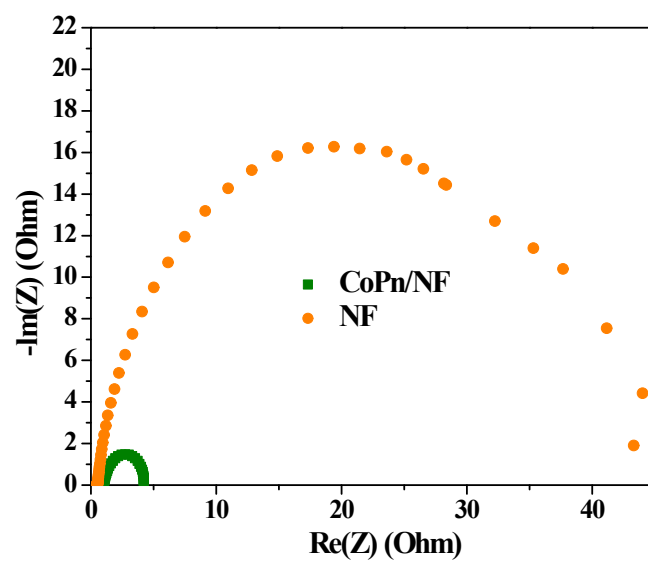


Figure S6. Nyquist plots for CoPn/NF and NF obtained from electrochemical impedance spectroscopic (EIS) measurements. The spectra were collected with an anodic polarization potential of 1.5 V vs. RHE.

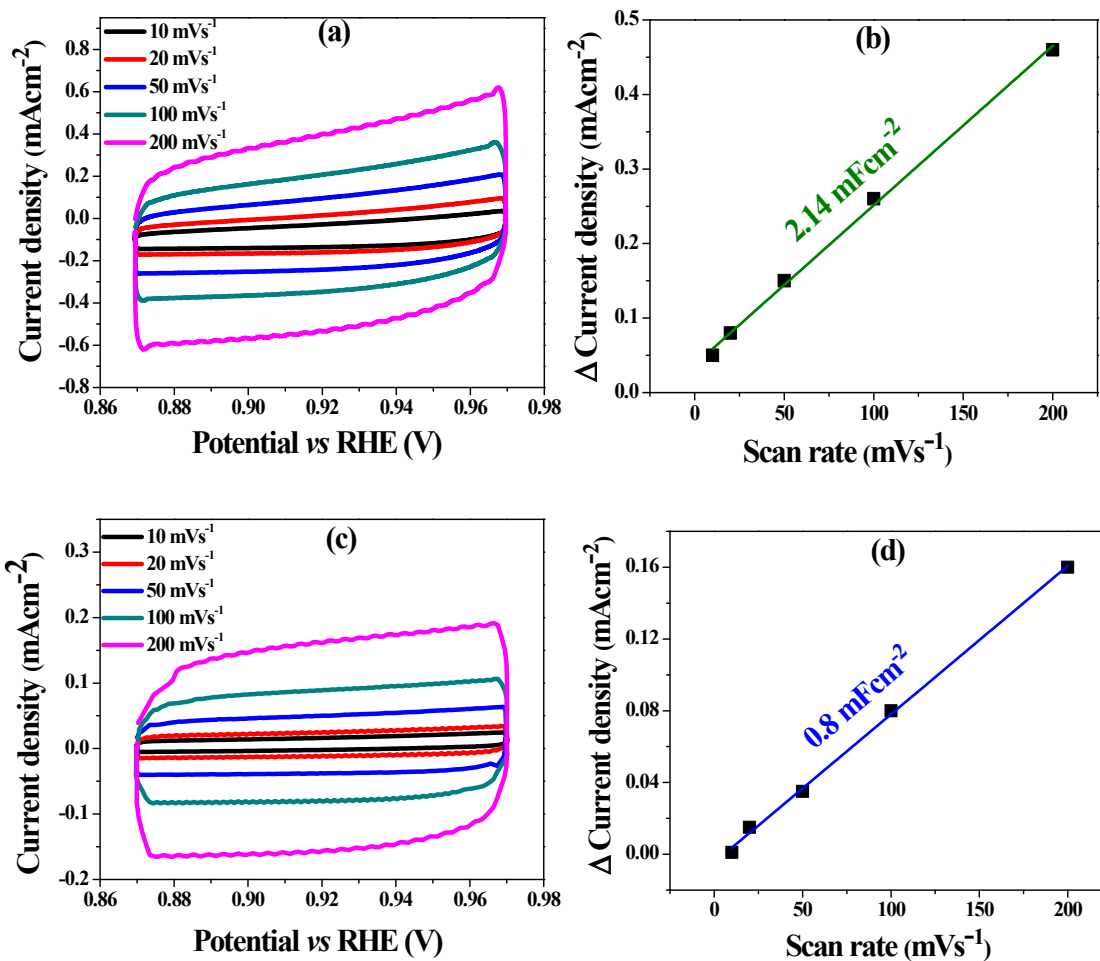


Figure S7. Measurement of electrochemical capacitance current of CoPn/NF (a) and NF (c), respectively, in the non-Faradaic potential range of 0.87 V to 0.97 V vs. RHE against different scan rates (10, 20, 50, 100, 200 mV/s) in 1 M aqueous KOH solution. (b) and (d) Half of the differences in current density variation ($\Delta J = (J_{\text{anodic}} - J_{\text{cathodic}})/2$) at a potential of 0.92 V vs. RHE plotted against scan rate fitted to a linear regression that allows the determination of double-layer capacitance (C_{dl}). The C_{dl} value attained for CoPn/NF was 2.14 mF cm⁻² while 0.8. mF cm⁻² was obtained for NF. The ECSA was then calculated by using the C_{dl} and the specific capacitance of the material (C_s) per unit area, and a value of 1.25 cm² for CoPn/NF and 0.47 cm² for NF was estimated.

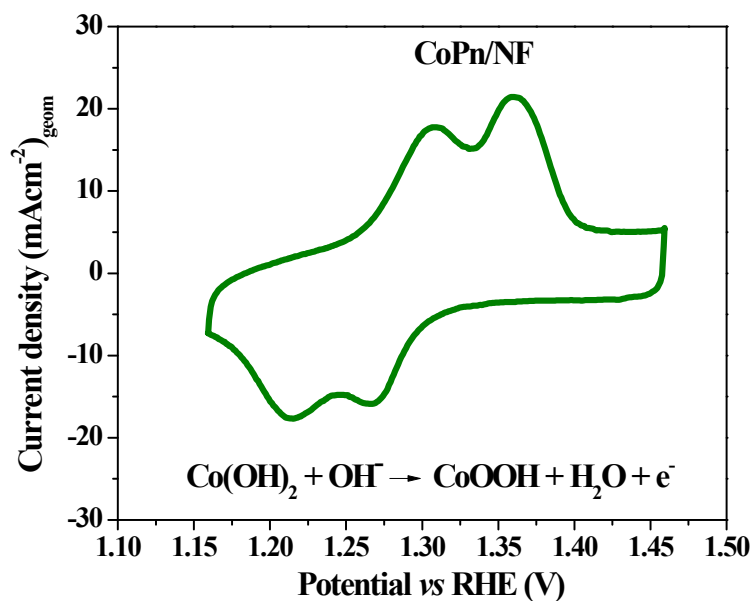


Figure S8. Cyclic voltammetry studies of CoPn/NF showing two redox peaks for the oxidation of Co^{2+} to Co^{3+} and Co^{4+} with applied anodic potential. Reaction conditions: 1 M aqueous KOH solution as the electrolyte and 5 mV s^{-1} scan rates.

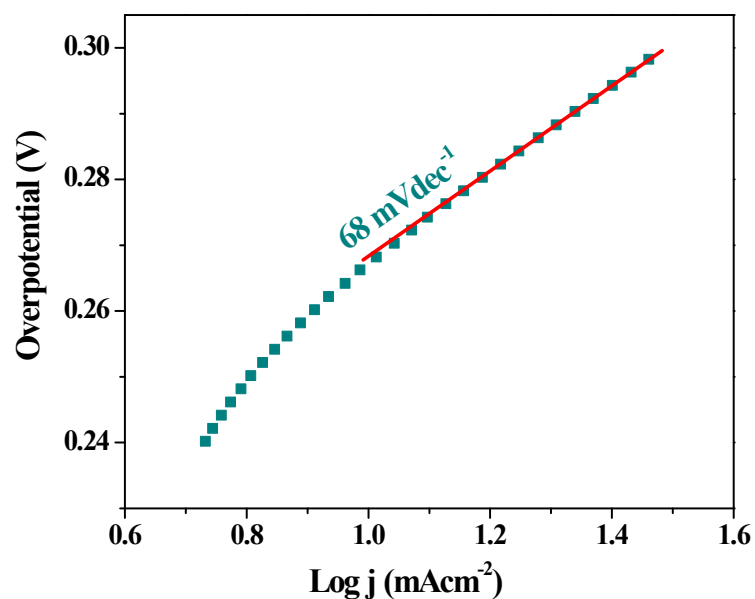


Figure S9. Tafel slope of CoPn/NF measured in 1 M aqueous KOH solution as the electrolyte and 1 mV s^{-1} scan rate.

Table S1. Comparison of the water oxidation activity of CoPn with transition metal-based catalysts in alkaline solution.

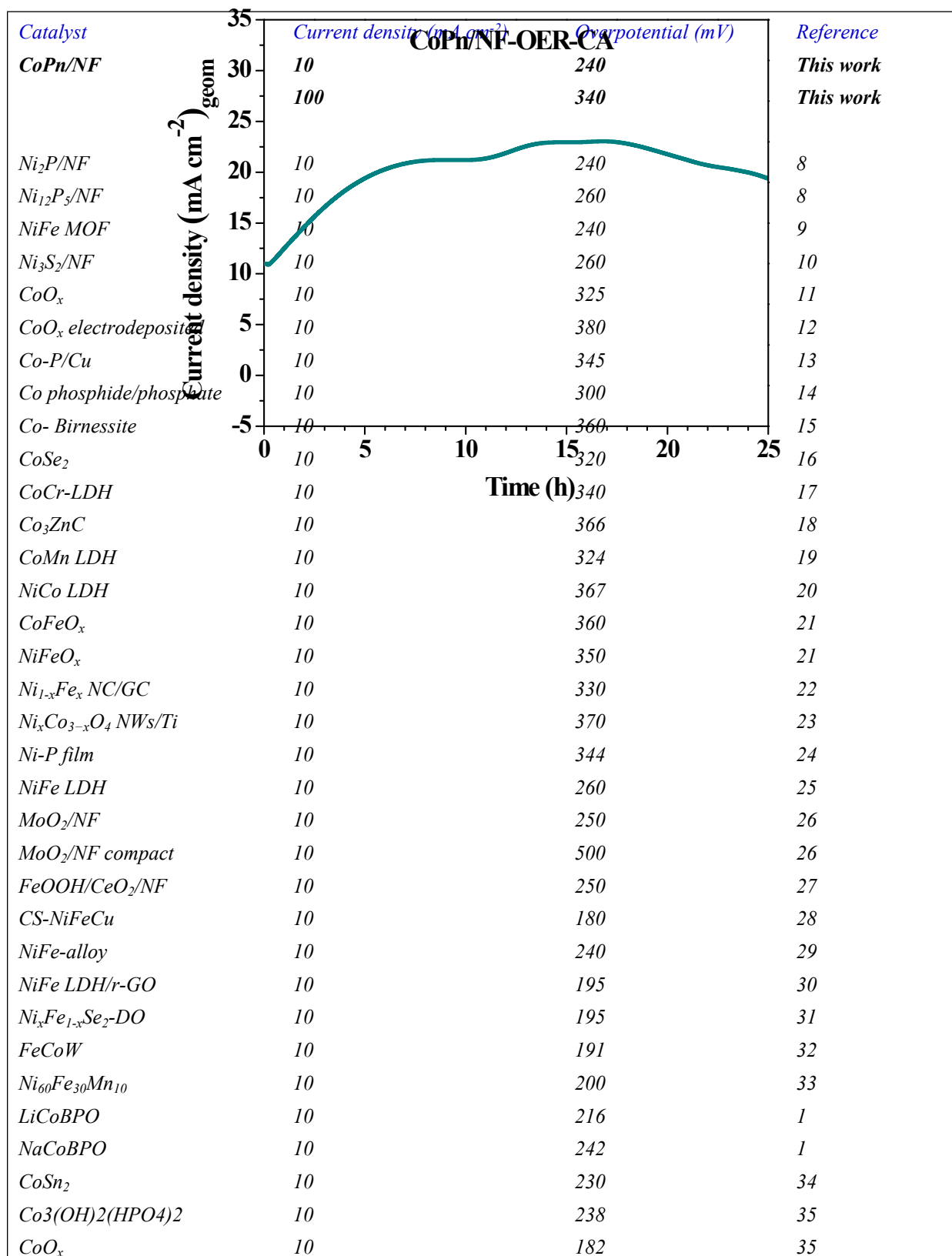


Table S2. Comparison of the hydrogen evolution activity of CoPn with transition metal-based catalysts in alkaline solution.

<i>Catalyst</i>	<i>Current density (mA cm⁻²)</i>	<i>Overpotential (mV)</i>	<i>Reference</i>
CoPn/NF	-10	144	This work
	-100	256	This work
<i>Cu₃P/NF</i>	<i>-10</i>	<i>105</i>	<i>36</i>
<i>NiFe/NiFe₂O₄/NF</i>	<i>-10</i>	<i>105</i>	<i>37</i>
<i>V/NF</i>	<i>-10</i>	<i>176</i>	<i>38</i>
<i>CoNiP/NF</i>	<i>-10</i>	<i>155</i>	<i>39</i>
<i>Co₉S₈-Ni_xS_y/NF</i>	<i>-10</i>	<i>163</i>	<i>40</i>
<i>NiS/NF</i>	<i>-10</i>	<i>150</i>	<i>41</i>
<i>Ni₃S₂@Ni</i>	<i>-10</i>	<i>195</i>	<i>42</i>
<i>CoS₂</i>	<i>-10</i>	<i>175</i>	<i>43</i>
<i>CoS₂</i>	<i>-10</i>	<i>145</i>	<i>44</i>
<i>CoN_x</i>	<i>-10</i>	<i>140</i>	<i>45</i>
<i>Co₉S₈@NOSC-900</i>	<i>-10</i>	<i>235</i>	<i>46</i>
<i>CoP/CC</i>	<i>-10</i>	<i>209</i>	<i>47</i>
<i>CoO_x/CN</i>	<i>-10</i>	<i>232</i>	<i>48</i>
<i>Ni₂P/FTO</i>	<i>-10</i>	<i>400</i>	<i>49</i>
<i>Ni-P foam</i>	<i>-10</i>	<i>135</i>	<i>50</i>
<i>NiFeP/Ni₂P</i>	<i>-10</i>	<i>183</i>	<i>51</i>
<i>Ni_xCo_{3-x}O₄/NiCo/NiCoO_x</i>	<i>-10</i>	<i>155</i>	<i>52</i>
<i>NiNiP</i>	<i>-10</i>	<i>130</i>	<i>53</i>
<i>Ni_{2.5}Co_{0.5}Fe/NF</i>	<i>-10</i>	<i>150</i>	<i>54</i>
<i>Ni₂P/GC</i>	<i>-20</i>	<i>250</i>	<i>55</i>
<i>Ni₅P₄ film</i>	<i>-10</i>	<i>180</i>	<i>56</i>
<i>NiCo₂S₄</i>	<i>-20</i>	<i>194</i>	<i>57</i>
<i>Ni₃FeN-NPs</i>	<i>-10</i>	<i>158</i>	<i>58</i>
<i>Zn_{0.76}Co_{0.24}S/CoS on Ti mesh</i>	<i>-10</i>	<i>200</i>	<i>59</i>
<i>Ni_{2.3%}CoS₂/CC</i>	<i>-10</i>	<i>150</i>	<i>60</i>
<i>LiCoBPO</i>	<i>-10</i>	<i>121</i>	<i>1</i>
<i>NaCoBPO</i>	<i>-10</i>	<i>207</i>	<i>1</i>
<i>Co₃(OH)₂(HPO₄)₂</i>	<i>-10</i>	<i>130</i>	<i>35</i>
<i>CoO_x</i>	<i>-10</i>	<i>87</i>	<i>35</i>
<i>CoSn₂</i>	<i>-10</i>	<i>103</i>	<i>34</i>

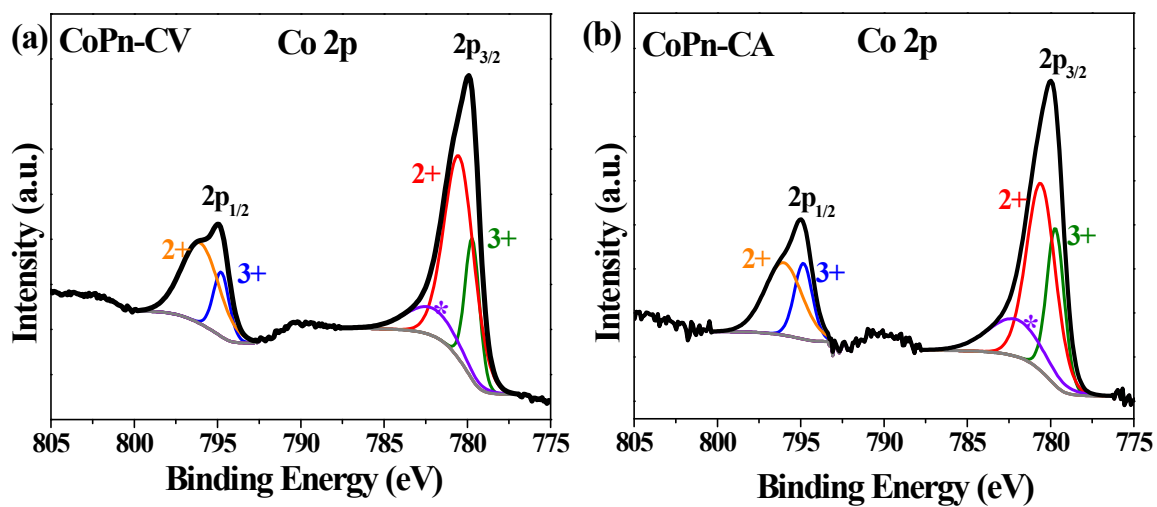


Figure S12. Co 2p XPS studies for the (a) CoPn after OER-CV and (b) CoPn after OER-CA measurements in 1 M aqueous KOH solution.

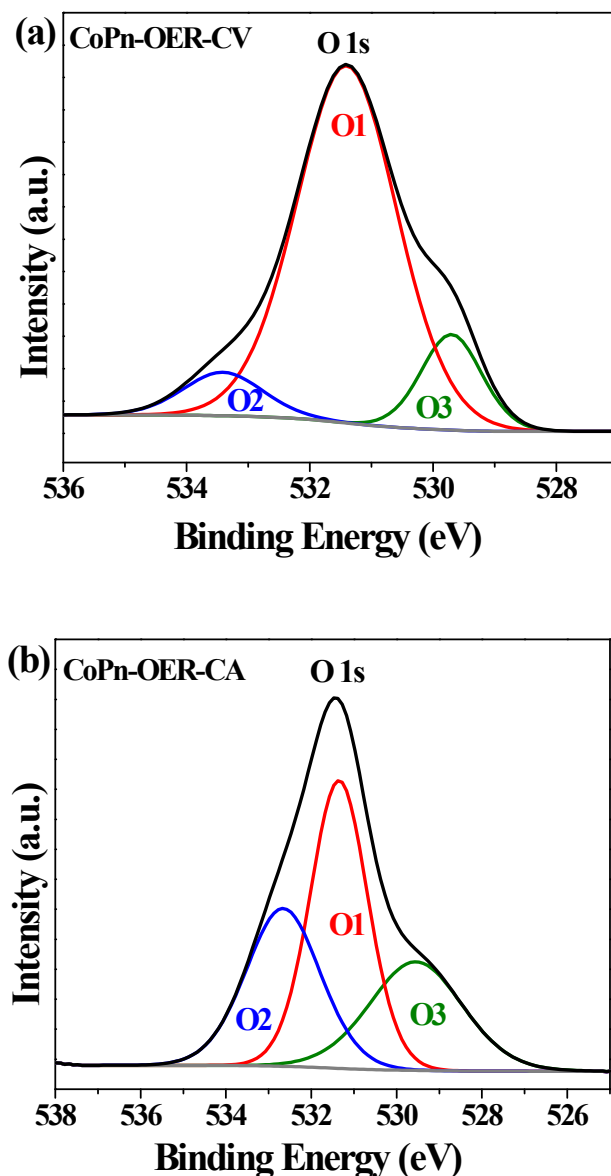


Figure S13. O 1s XPS studies for the (a) CoPn after OER-CV and (b) CoPn after OER-CA measurements in 1 M aqueous KOH solution. The change in the O1s spectra is significant after the electrolysis in an alkaline solution. In fresh CoPn, O 1s spectrum was deconvoluted into two peaks O1 at ~531.2 eV corresponding to P-O-Co moiety and O2 at ~532.0 eV representing the oxygen from the water (see Figure S7).⁷ After the electrochemical measurements, a third peak O3 is generated at 529.5 eV indicating the formation of metal-oxygen bonds.⁴⁴ This result clearly describes the transformation of CoPn to the hydroxide-oxyhydroxide structure during water oxidation in alkaline medium. The other two peaks (531.4 eV and 533.4 eV after CV) and (531.4 eV and 532.7 eV after CA) represent hydroxylation and hydration during electrochemical processes.⁴⁴

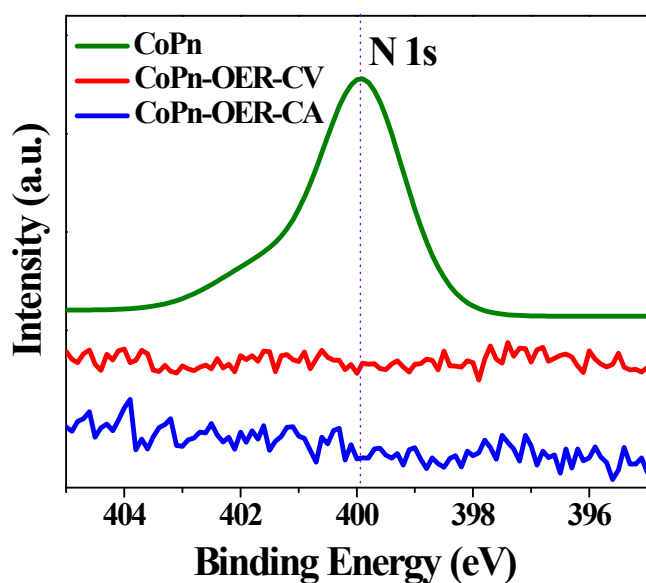


Figure S14. N 1s XPS studies for the CoPn after anodic oxygen evolution reactions (CV and CA) in 1 M aqueous KOH solution and compared with the fresh sample. After the electrochemical measurements, the peaks from N 1s completely disappeared, indicating a structural transformation.

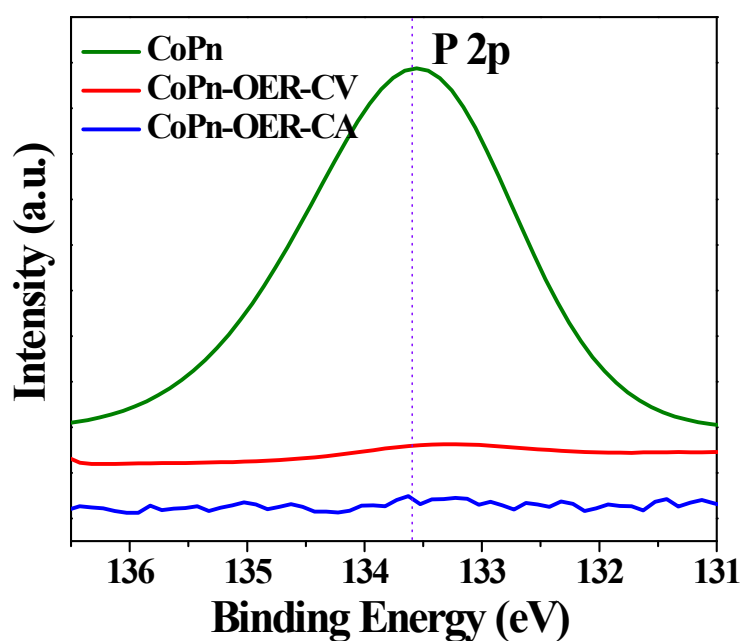


Figure S15. P 2p XPS studies for the CoPn after anodic oxygen evolution reactions (CV and CA) in 1 M aqueous KOH solution compared with the fresh sample. After the electrochemical measurements, the peaks from P 2p completely disappeared, indicating a structural transformation.

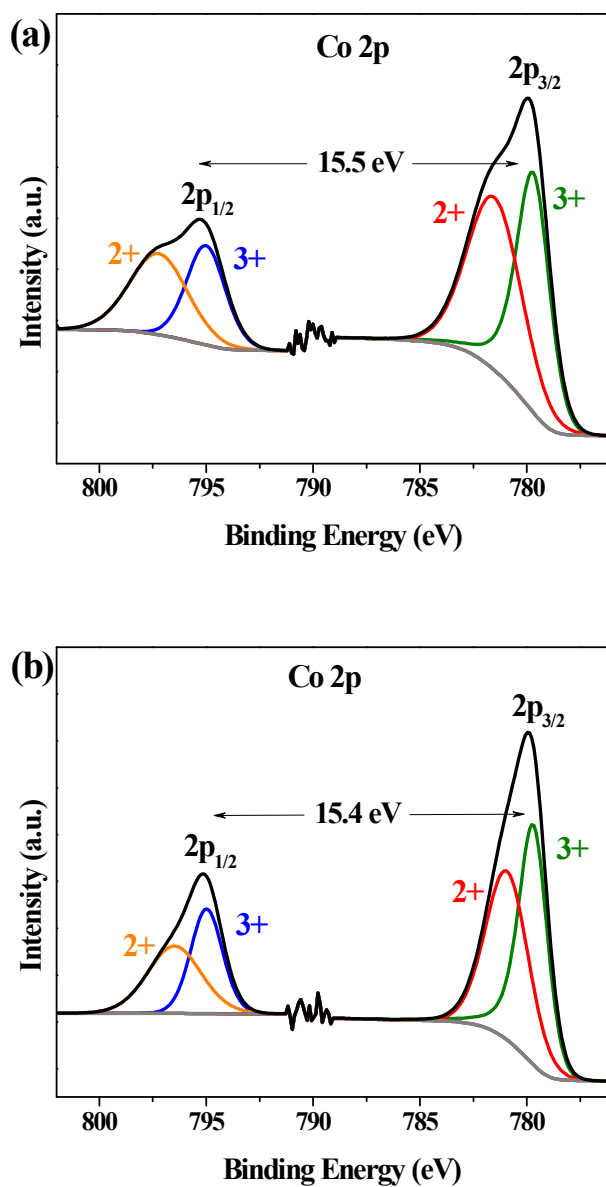


Figure S16. Co 2p XPS studies for the CoPn after cathodic hydrogen evolution reactions (a) CV and (b) CA in 1 M aqueous KOH solution. After the electrochemical measurements, the oxidation state of cobalt is increased to form mixed valent Co^{II/III} species.

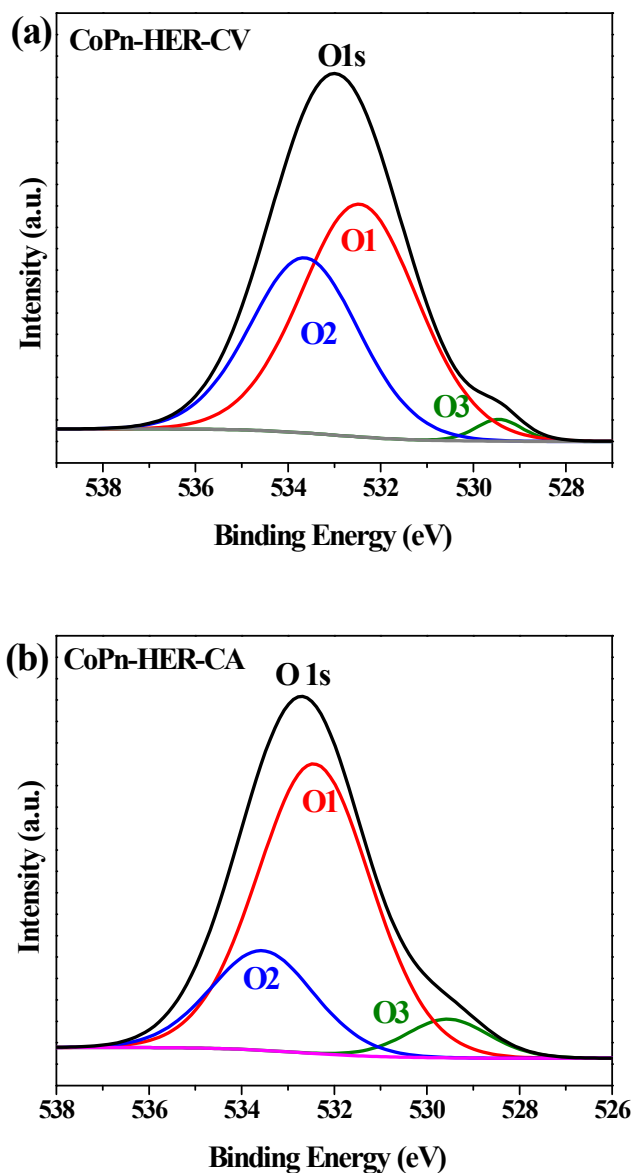


Figure S17. O 1s XPS studies for the (a) CoPn after HER-CV and (b) CoPn after HER-CA measurements in 1 M aqueous KOH solution. The change in the O 1s spectra is significant after the electrolysis in alkaline solution. In fresh CoPn, O 1s spectrum was deconvoluted into two peaks O1 at ~531.2 eV corresponding to P-O-Co moiety and O2 at ~532.0 eV representing the oxygen from the water (see Figure S7).¹ After electrochemical measurements, a third peak O3 is generated at 529.5 eV indicating the formation of metal-oxygen bonds.¹ This result clearly describes the transformation of CoPn to the new structure during hydrogen evolution in alkaline medium. The other two peaks (532.5 and 533.7 eV) appear due to the hydration during the electrochemical processes.

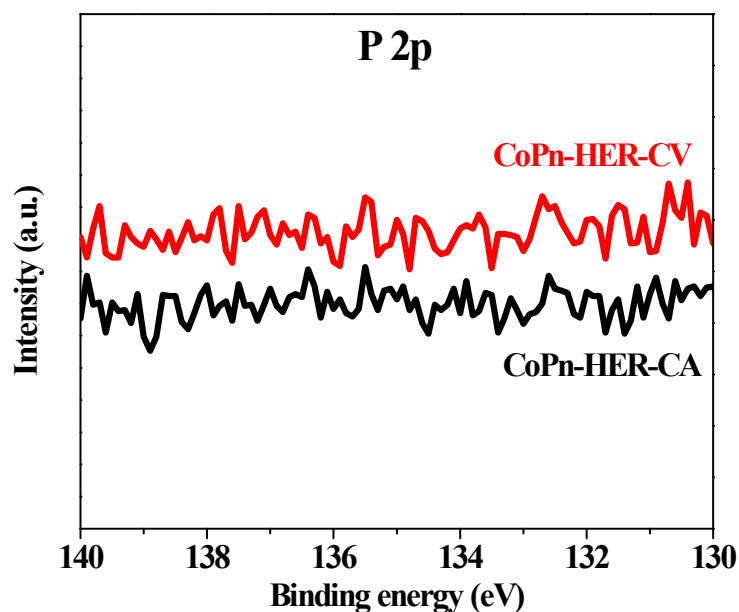


Figure S18. P 2p XPS studies for the CoPn after cathodic hydrogen evolution reactions (CV and CA) in 1 M aqueous KOH solution. After the electrochemical measurements, the peaks from P 2p completely disappeared, indicating complete loss of phosphorous from CoPn due to structural transformation at the cathode during HER.

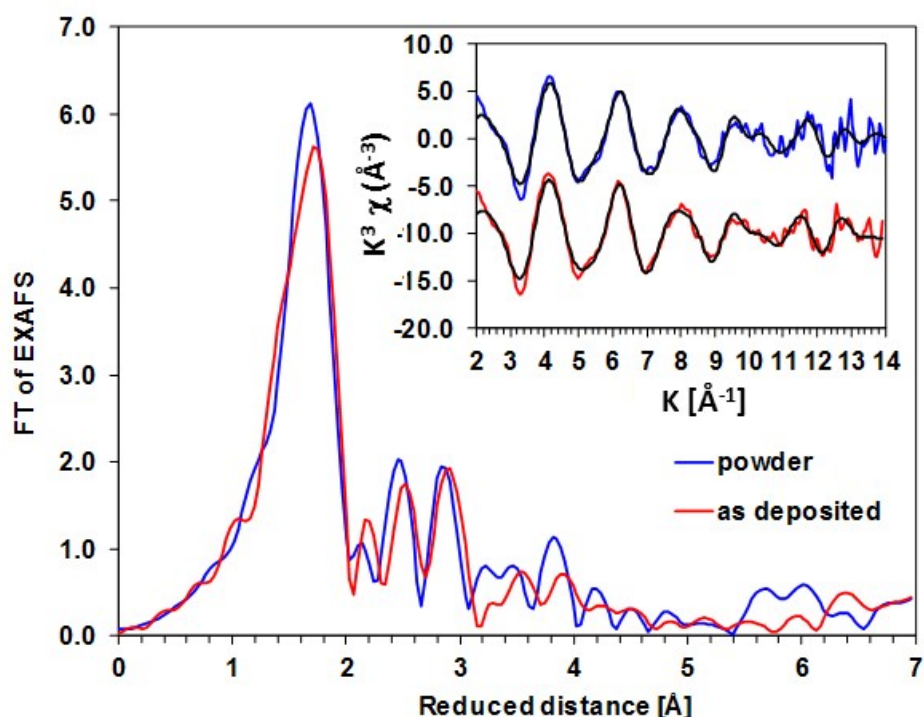


Figure S19. Fourier transformed (FT) EXAFS spectra from the CoPn powder and as-deposited material. Inset: original EXAFS spectra and simulations (black lines). Simulation parameters are shown in Table S3.

Table S3. The parameters indicated with an asterisk (*) were fixed during the simulation. The sum of the coordination numbers (N) for the first two Co-O shells was fixed to 6.

Peak no.	Atoms	N	R (Å)	σ (Å)	R _f (%)
Cobalt phosphonate powder					
1	Co–O	3.0 ± 0.9	2.01 ± 0.03	0.057 ± 0.022	19.9
1	Co–O	3.0	2.11 ± 0.03		
2	Co–Co	0.6 ± 0.2	2.87 ± 0.02	0.063*	
3	Co–P	2.1 ± 0.5	3.26 ± 0.02	0.063*	
4	Co–Co	0.9 ± 0.4	4.12 ± 0.03	0.063*	
Cobalt phosphonate as deposited on the electrode					
1	Co–O	2.0 ± 0.3	1.97 ± 0.02	0.057 ± 0.022	18.3
1	Co–O	4.0	2.10 ± 0.01		
2	Co–Co	0.5 ± 0.2	2.92 ± 0.02	0.063*	
3	Co–P	2.3 ± 0.5	3.28 ± 0.01	0.063*	
4	Co–Co	0.4 ± 0.5	4.16 ± 0.06	0.063*	

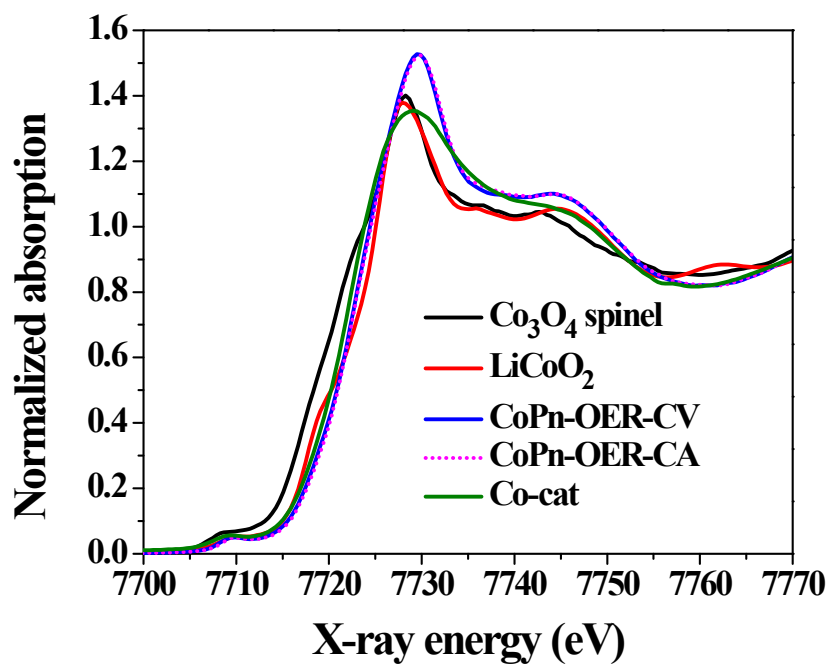


Figure S20. Co K-edge XANES spectra of CoPn after water oxidation (CV and CA) compared with those of other catalysts.

Table S4. The parameters indicated with an asterisk (*) were fixed during the simulation. The superscript MS indicates that multiple scattering paths were considered in the simulation. In the first column, the assignment of the simulated distances to reference Co structures is shown. In the second simulation approach, the coordination numbers are fixed according to the ideal crystal structure of spinel or layered cobalt oxide. The interatomic distances according to the spinel crystal structure are given in parentheses. The Debye-Waller factors of all oxygen shells and for the short-distance Co shells are kept the same.

Structure	Atoms	N	R (Å)	σ (Å)	Contribution (%)	R _f (%)
After CV at OER potentials, simulation approach 1						
CoCat/Co ₃ O ₄	Co–O	6.1 ± 0.5	1.90 ± 0.01	0.046 ± 0.007	100% (simulated as single phase)	15.4
CoCat/Co ₃ O ₄	Co–Co	6.6 ± 0.7	2.85 ± 0.01	0.053 ± 0.005		
Co ₃ O ₄	Co–Co	4.6 ± 0.9	3.44 ± 0.01	0.063*		
CoCat	Co–O	9.2 ± 3.8	3.60 ± 0.02	0.036 ± 0.024		
CoCat	Co–Co	4.9 ± 1.5	2 • cos(30°) • 2.85	0.063*		
CoCat	Co–Co ^{MS}	4.9 ± 0.7	2 • 2.85	0.063*		
After CA at OER potentials, simulation approach 1						
CoCat / Co ₃ O ₄	Co–O	6.2 ± 0.6	1.90 ± 0.01	0.053 ± 0.007	100% (simulated as single phase)	16.5
CoCat / Co ₃ O ₄	Co–Co	6.2 ± 0.7	2.84 ± 0.01	0.053 ± 0.005		
Co ₃ O ₄	Co–Co	4.0 ± 0.9	3.43 ± 0.02	0.063*		
CoCat	Co–O	8.9 ± 3.8	3.60 ± 0.02	0.042 ± 0.024		
CoCat	Co–Co	3.4 ± 1.5	2 • cos(30°) • 2.85	0.063*		
CoCat	Co–Co ^{MS}	4.4 ± 0.7	2 • 2.85	0.063*		
After CV at OER potentials, simulation approach 2						
Co ₃ O ₄	Co–O	5.33*	1.93 ± 0.23 (1.94)	0.042 ± 0.028	21.4 ± 0.03	13.6
	Co–Co	4*	2.75 ± 0.03 (2.78)	0.032 ± 0.006		
	Co–Co	8*	3.43 ± 0.01 (3.37)	0.032 ± 0.006		
	Co–O	8*	3.58 ± 0.08 (3.50)	0.042 ± 0.028		
CoCat	Co–O	6*	1.89 ± 0.04	0.042 ± 0.028	78.6 ± 0.03	
	Co–Co	6*	2.85 ± 0.01	0.032 ± 0.006		
	Co–Co	6*	2 • cos(30°) • 2.85	0.061 ± 0.005		
	Co–Co ^{MS}	6*	2 • 2.85			
After CA at OER potentials, simulation approach 2						
Co ₃ O ₄	Co–O	5.33*	1.91 ± 0.03 (1.94)	0.051 ± 0.047	20.6 ± 0.05	15.0
	Co–Co	4*	2.76 ± 0.04 (2.78)	0.039 ± 0.006		
	Co–Co	8*	3.42 ± 0.02 (3.37)	0.039 ± 0.006		
	Co–O	8*	3.56 ± 0.11 (3.50)	0.051 ± 0.047		
CoCat	Co–O	6*	1.89 ± 0.22	0.051 ± 0.047	79.4 ± 0.05	
	Co–Co	6*	2.84 ± 0.01	0.039 ± 0.006		
	Co–Co	6*	2 • cos(30°) • 2.85	0.066 ± 0.005		
	Co–Co ^{MS}	6*	2 • 2.85			

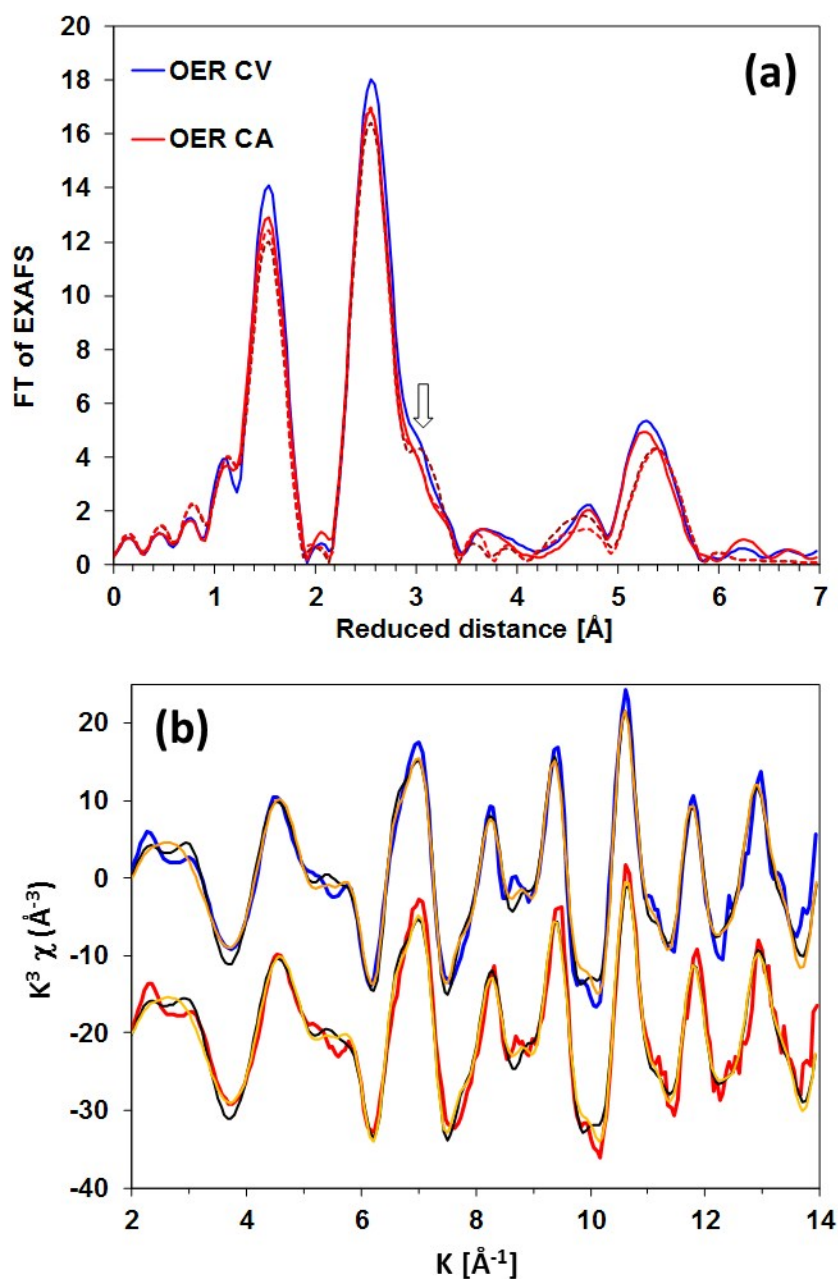


Figure S21. EXAFS spectra of the CoPn after cycling (CV) and at CA relevant to OER. (a) FT of EXAFS indicated that the same structure is formed after CV and CA (25 h at 1.56V vs. RHE). Solid lines: experimental data, dashed lines: simulations. The error indicates the shoulder suggesting the presence of additional phase (b) k-space EXAFS spectra. Colored lines: experimental spectra; thin black lines: simulated spectra according to the simulation approach 1; orange lines: simulated spectra according to the simulation approach 2. Simulation parameters are given in Table S4.

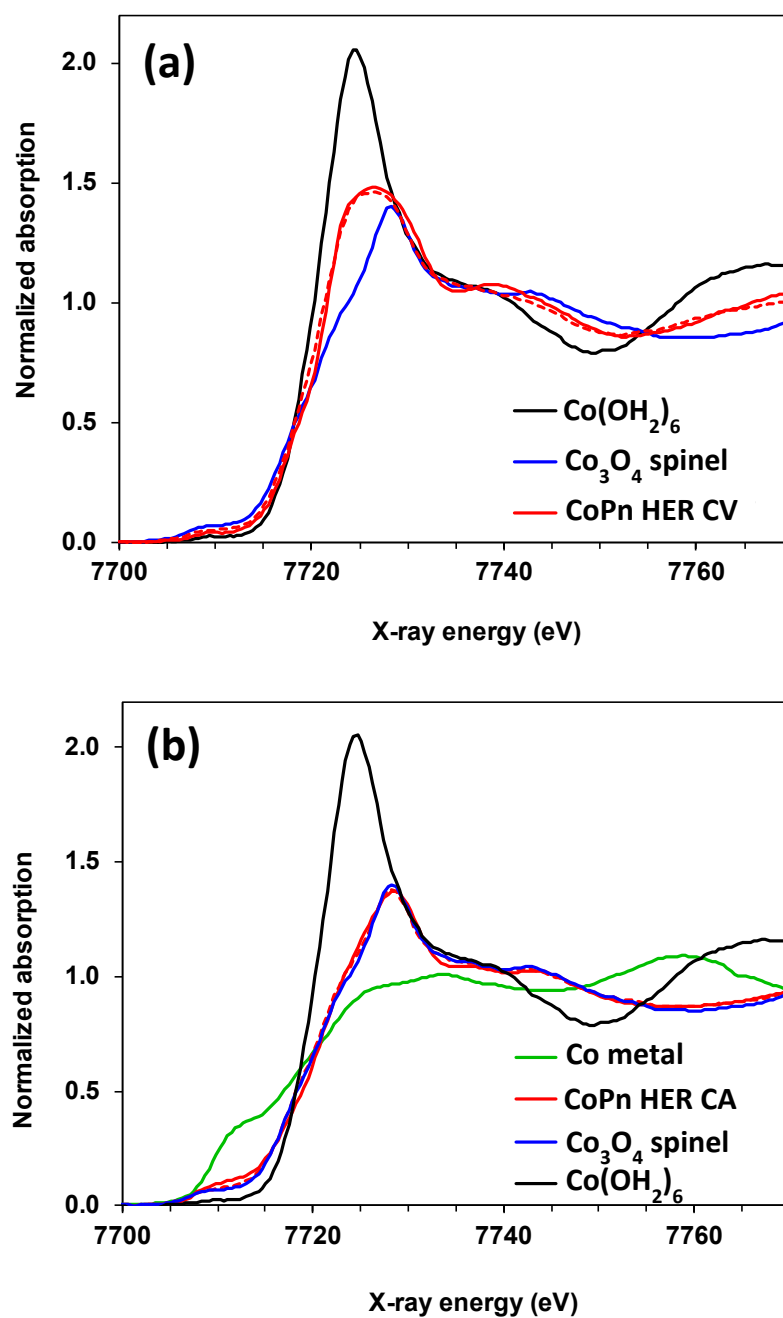


Figure S22. Simulation as a linear combination of reference spectra of the edge spectra of Co phosphonate used as H_2 evolution catalysts in an electrochemical cell (a) after CVs and (b) after application of constant potential. The red dashed line represents the simulation as a linear combination of the spectra.

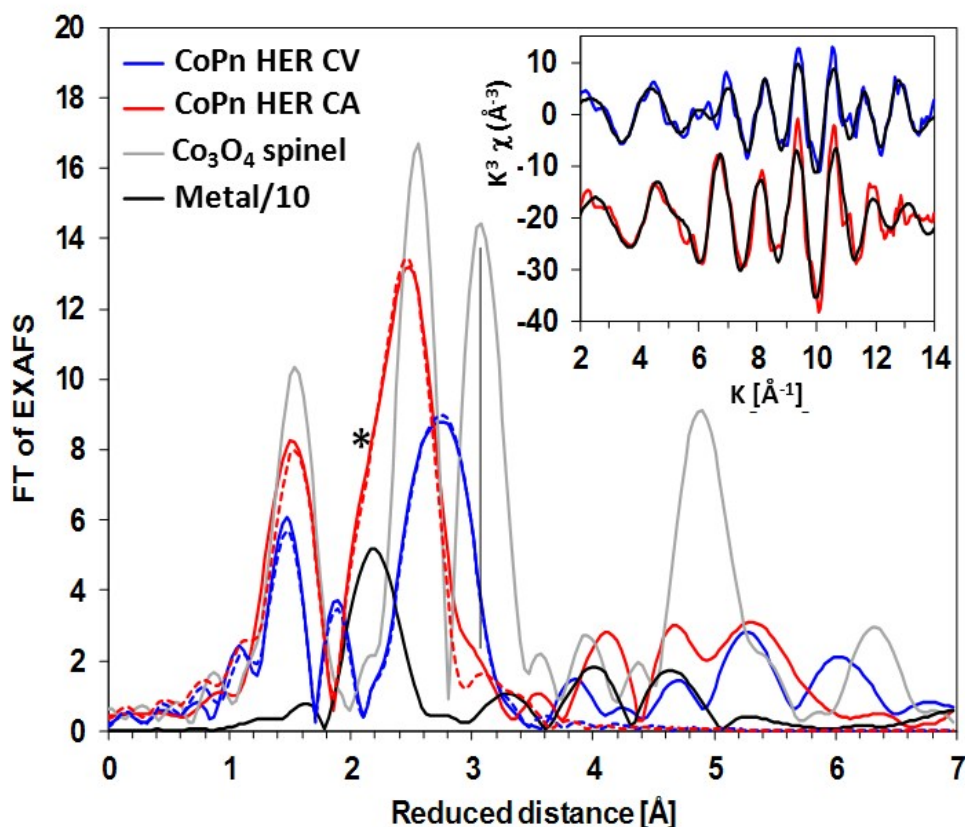


Figure S23. FT of EXAFS of CoPn after hydrogen evolution reaction. Spectra from Co spinel and Co metal are shown to illustrate the contribution of different structural motifs from these references to the resulting structures. The simulation parameters are shown in Table S5. The FT amplitude for the metallic spectrum is reduced by a factor of 10 for better representation. The asterisk (*) indicates the shoulder in the second peak in the CA catalyst that results from the metallic contribution. The contribution of the third FT peak (mono μ -oxo bridges, indicated with a vertical line) from the spinel structure is lower than expected. Inset: original EXAFS spectra and simulations (black lines).

Table S5. The parameters indicated with an asterisk (*) were fixed during the simulation. In the first column, a tentative assignment of the simulated distances to reference Co structures is shown.

structure	atoms	N	R (Å)	σ (Å)	R _f (%)
After CV at HER potentials					
Co ²⁺	Co–O	2.7 ± 0.2	2.11 ± 0.01	0.050 ± 0.004	4.5
Co ₃ O ₄	Co–O	3.4 ± 0.2	1.90 ± 0.01		
Co ₃ O ₄	Co–Co	2.9 ± 0.1	2.84 ± 0.01	0.063*	
-	Co–Co	4.1 ± 0.2	3.16 ± 0.01	0.063*	
Co ₃ O ₄	Co–Co	1.0 ± 0.2	3.42 ± 0.01	0.063*	
After CA at HER potentials					
Co ₃ O ₄	Co–O	4.4 ± 0.7	1.90 ± 0.01	0.057 ± 0.007	14.1
Co ₃ O ₄	Co–Co	5.0 ± 0.4	2.84 ± 0.01	0.063*	
Co ₃ O ₄	Co–Co	1.3 ± 0.6	3.45 ± 0.03	0.063*	
metal	Co–Co	2.8 ± 0.3	2.51 ± 0.01	0.063*	

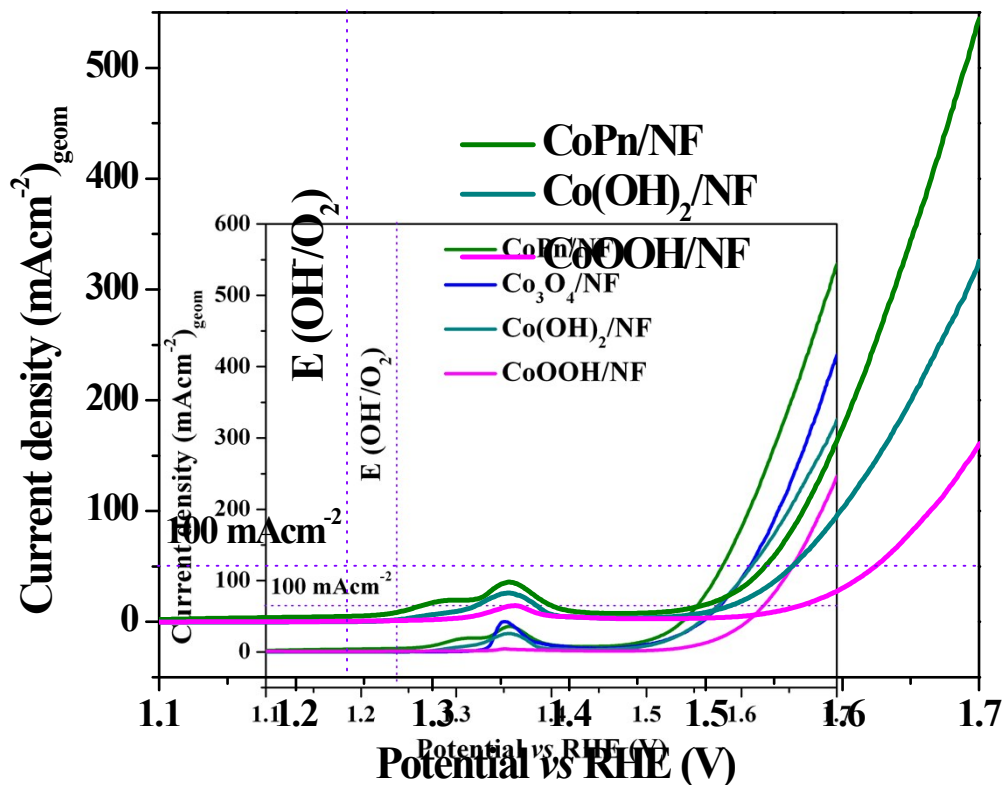


Figure S24. Linear sweep voltammogram (LSV) profiles of alkaline oxygen evolution reactions with cobalt-based catalysts (resulted from the active structures of CoPn during OER) compared with CoPn/NF. Reaction conditions: 1 M aqueous KOH solution as the electrolyte and 5 mVs^{-1} scan rate. The Co_3O_4 and Co(OH)_2 catalysts were purchased commercially whereas CoOOH was synthesized using a literature reported procedure.¹

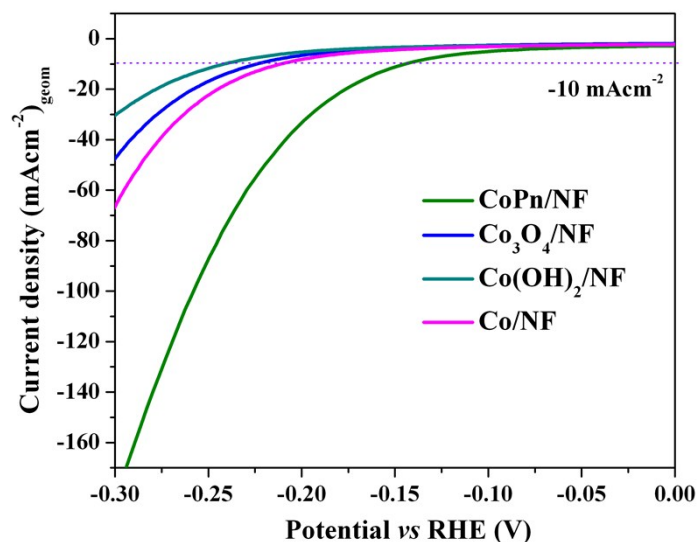


Figure S25. Linear sweep voltammogram (LSV) profiles of alkaline hydrogen evolution reactions with cobalt-based catalysts (resulted from the active structures of CoPn during HER) compared with CoPn/NF. Reaction conditions: 1 M aqueous KOH solution as the electrolyte and 5 mVs^{-1} scan rate. The Co_3O_4 and Co catalysts were purchased commercially whereas CoOOH was synthesized using a literature reported procedure.¹

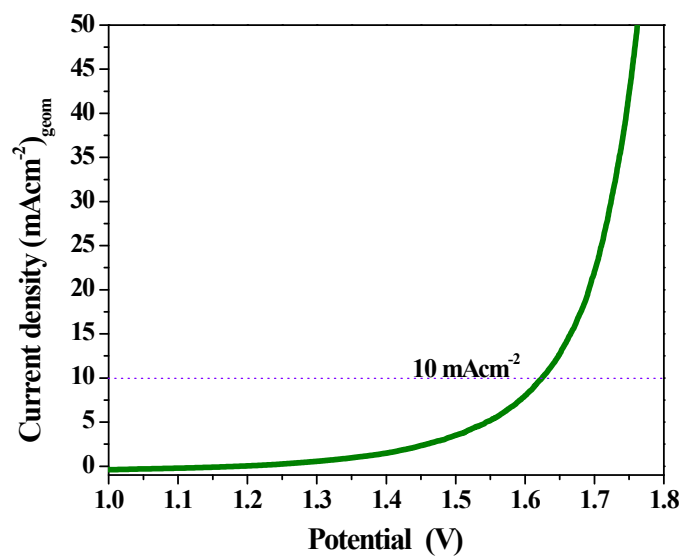


Figure S26. Overall water splitting in a two-electrode CoPn@NF//CoPn@NF system in 1 M aqueous KOH solution with a scan rate of 5 mV s^{-1} .

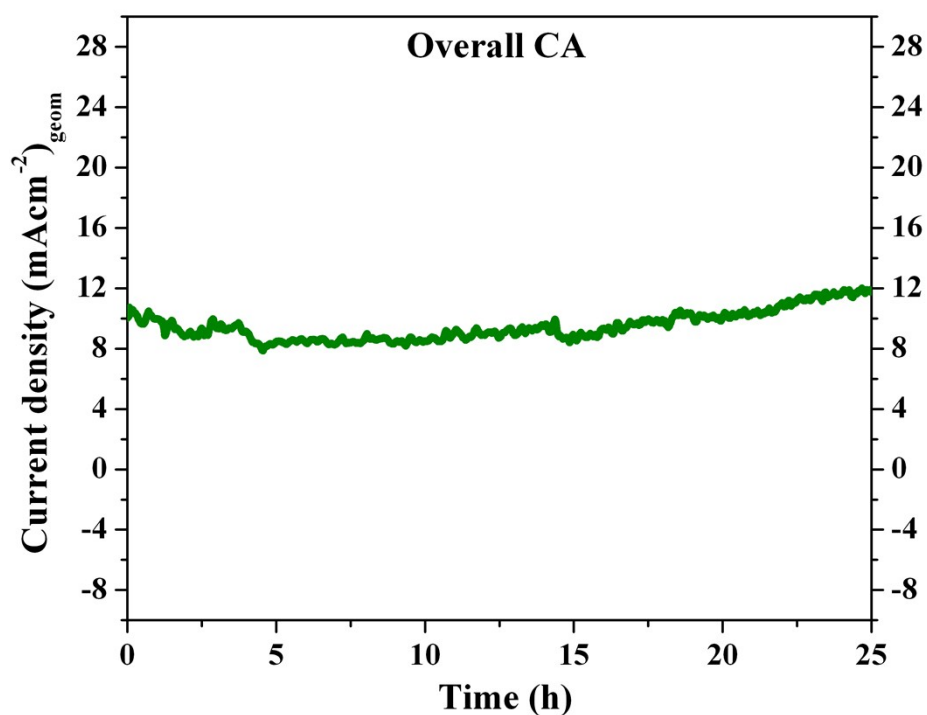


Figure S27. CA for the overall water splitting with cobalt phosphonate (CoPn) supported on Ni nanofoam in 1 M aqueous KOH solution at a constant potential of 1.65 V vs. RHE.

References

1. P. W. Menezes, A. Indra, I. Zaharieva, C. Walter, S. Loos, S. Hoffmann, R. Schlögl, H. Dau and M. Driess, *Energy Environ. Sci.*, 2019, **12**, 988-999.
2. a) A. L. Ankudinov, B. Ravel, J. J. Rehr, S. D. Conradson, *Phys.Rev. B: Condens. Mater. Phys.*, 1998, **58**, 7565-7576; b) J. J. Rehr and R. C. Albers, *Rev. Mod. Phys.*, 2000, **72**, 621-654.
3. a) I. Zaharieva, P. Chernev, M. Risch, K. Klingan, M. Kohlhoff, A. Fischer and H. Dau, *Energy Environ. Sci.*, 2012, **5**, 7081-7089; b) M. Risch, V. Khare, I. Zaharieva, L. Gerencser, P. Chernev, and H. Dau, *J. Am. Chem. Soc.*, 2009, **131**, 6936-6937.
4. S. Trasatti, and O. A. Petrii, *J. Electroanalytical Chem.*, 1992, **327**, 353-376.
5. a) C. C. L. McCrory, S. Jung, J. C Peters, and T. F. Jaramillo, *J. Am. Chem. Soc.*, 2013, **135**, 16977-16987; b) Y. Yoon, B. Yan, and Y. Surendranath, *J. Am. Chem. Soc.*, 2018, **140**, 2397-2400; c) Q. Kang, L. Vernisse, R. C. Remsing, A. C. Thenuwara, S. L. Shumlas, I. G. McKendry, M. L. Klein, B. Eric, M. J. Zdilla and D. R. Strongin, *J. Am. Chem. Soc.*, 2017, **139**, 1863-1870.
6. Y. Zhu, T. Ren and Z. Yuan, *Nanoscale*, 2014, **6**, 11395-11402.
7. P. W. Menezes, A. Indra, A. Bergmann, P. Chernev, C. Walter, H. Dau, P. Strasser and M. Driess, *J. Mater. Chem. A*, 2016, **4**, 10014-10022.
8. P. W. Menezes, A. Indra, C. Das, C. Walter, C. Gobel, V. Gutkin, D. Schmeißer and M. Driess, *ACS Catal.*, 2017, **7**, 103-109.
9. J. Duan, S. Chen and C. Zhao, *Nat. Commun.*, 2017, **8**, 15341.
10. L. L. Feng, G. Yu, G. D. Li, H. Li, Y. Sun, T. Asefa, W. Chen and X. Zou, *J. Am. Chem. Soc.*, 2015, **137**, 14023-14026.
11. A. Indra, P. W. Menezes, C. Das, C. Goebel, M. Tallarida, D. Schmeißer and M. Driess, *J. Mater. Chem. A.*, 2017, **5**, 5171-5177.
12. M. D. Merrill and R. C. Dougherty, *J. Phy. Chem. C*, 2008, **112**, 3655-3666.
13. N. Jiang, B. You, M. Sheng and Y. Sun, *Angew. Chem. Int. Ed.*, 2015, **54**, 6251-6254.
14. Y. Yang, H. L. Fei, G. D. Ruan and J. M. Tour, *Adv. Mater.*, 2015, **27**, 3175-3180.
15. A. C. Thenuwara, S. L. Shumlas, N. H. Attanayake, Y. V. Aulin, L.G. McKendry Q. Qiao, Y. Zhu, E. Borguet, M. J. Zdilla and D. R. Strongin, *ACS Catal.*, 2016, **6**, 7739-7743.
16. Y. W Liu, H. Cheng, M. Lyu, S. Fan, Q. Zhang, W. Liu, Y. Zhi, C. Wang, C. Xiao, S. Wei, B. Ye and Y. Xie *J. Am. Chem. Soc.*, 2012, **136**, 15670-15675.
17. C. L. Dong, X. Yuan, X. Wang, X. Liu, W. Dong, R. Wang, Y. Duan and F. Huang, *J. Mater. Chem. A*, 2016, **4**, 11292-11298.
18. J. W. Su, G. Xia, R. Li, Y. Yang, J. Chen, R. Shi, P. Jiang and Q. Chen, *J. Mater. Chem. A*, 2016, **4**, 9204-9212.

19. F. Song, X. and L. Hu, *J. Am. Chem. Soc.*, 2014, **136**, 16481-16484.
20. H. F. Liang, F. Meng, M. Caban-Acevedo, L. Li, A. Forticaux, L. Xiu, Z. Wang and S. Jin, *Nano Lett.*, 2015, **15**, 1421-1427.
21. C. C. L. McCrory, S. Jung, J. C. Peters, and T. F. Jaramillo, *J. Am. Chem. Soc.*, 2013, **135**, 16977-16987.
22. X. Zhang, H. Xu, X. Li, Y. Li, T. Yang and Y. Liang, *ACS Catal.*, 2016, **6**, 580-588.
23. Y. G. Li, P. Hasin and Y. Y. Wu, *Adv. Mater.*, 2010, **22**, 1926-1929.
24. N. Jiang, B. You, M. L. Sheng and Y. J. Sun, *ChemCatChem*, 2016, **8**, 106-112.
25. B. M. Hunter, J. D. Blakemore, M. Deimund, H.B. Gray, J. R. Winkler and A. M. Müller, *J. Am. Chem. Soc.*, 2014, **136**, 13118-13121.
26. Y. S. Jin, H. Wang, J. Li, X. Yue, Y. Han, P. K. Shen and Y. Cui, *Adv. Mater.*, 2016, **28**, 3785-3790.
27. J. X. Feng, S. H. Ye, H. Xu, Y. X. Tong and G. R. Li, *Adv. Mater.*, 2016, **28**, 4698-4703.
28. P. Zhang, L. Li, D. Nordlund, H. Chen, L. Fan, B. Zhang, X. Sheng, Q. Daniel and L. Sun, *Nat. Commun.*, 2018, **9**, 381.
29. S. Loos, I. Zaharieva, P. Chernev, A. Lißner and H. Dau, *ChemSusChem*, 2019, **12**, 1966-1976
30. X. Long, J. Li, S. Xiao, K. Yan, Z. Wang, H. Chen and S. Yang, *Angew. Chem. Int. Ed.*, 2014, **53**, 7584-7588.
31. X. Xu, F. Song and X. Hu, *Nature Commun.*, 2016, **7**, 12324.
32. B. Zhang, X. Zheng, O. Voznyy, R. Comin, M. Bajdich, M. García-Melchor, L. Han, J. Xu, M. Liu, L. Zheng, F. García de Arquer, P. Dinh and C. T. Fan, *Science*, 2016, **352**, 333-337
33. E. Detsi, J. B. Cook, B. K. Lesel, C. L. Turner, Y. -L. Liang, S. Robbenolta and S. H. Tolbert, *Energy Environ. Sci.*, 2016, **9**, 540-549.
34. P. W. Menezes, C. Panda, S. Garai, C. Guet, A. Walter and M. Driess, *Angew. Chem. Int. Ed.*, 2018, **57**, 15237-15242
35. P. W. Menezes, C. Panda, C. Walter, M. Schwarze and M. Driess, *Adv. Funct. Mater.*, 2019, 1808632.
36. A. Han, , H. Y. Zhang, R. H. Yuan, H. X. Ji and P. Du, *ACS Appl. Mater. Interfaces*, 2017, **9**, 2240-2248.
37. C. L. Xiao, Y. B. Li, X. Y. Lu and C. Zhao, *Adv. Funct. Mater.*, 2016, **26**, 3515-3523.
38. Y. Yu, P. Li, X. Wang, W. Gao, Z. Shen, Y. Zhu, S. Yang, W. Song and K. Ding, *Nanoscale*, 2016, **8**, 10731-10738.
39. A. Han, H. Chen, H. Zhang, Z. Sun and P. J. Du, *Mater. Chem. A*, 2016, **4**, 10195-10202.
40. D. Ansovini,; C. J. J. Lee, C. S. Chua, L. T. Ong, H. R. Tan, W. R. Webb, R. Raja and Y. F.J. Lim, *Mater. Chem. A*, 2016, **4**, 9744-9749.

41. W. Zhu, X. Yue, W. Zhang, S. Yu, Y. Zhang, J. Wan and J. L. Wang, *Chem. Commun.*, 2016, **52**, 1486-1489.
42. C. B. Quyang, X. Wang, C. Wang, X. Zhang, J. Wu, Z. L. Ma, S. Dou and S. Wang, *Electrochim. Acta*, 2015, **174**, 297-301.
43. Y. J. Sun, C. Liu, D. C. Grauer, J. Yano, J. R. Long, P. Yang and C. J. Chang, *J. Am. Chem. Soc.*, 2013, **135**, 17699-17702.
44. M. S. Faber, R. Dziejic, M. A. Lukowski, N. S. Kaiser, Q. Ding and S. Jin, *J. Am. Chem. Soc.*, 2014, **136**, 10053-10061.
45. H. W. Liang, S. Brüller, R. Dong, J. Zhang, X. Feng and K. Müllen, *Nat. Commun.*, 2015, **6**, 7992.
46. S. C. Huang, Y. Meng, S. He, A. Goswami, Q. Wu, J. Li, S. Tong, T. Asefa and M. Wu, *Adv. Funct. Mater.*, 2017, **27**, 1606585.
47. J. Q. Tian, Q. Liu, A. M. Asiri and X. P. Sun, *J. Am. Chem. Soc.*, 2014, **136**, 7587-7590.
48. H. Y. Jin, J. Wang, D. Su, Z. Wei, Z. Pang and Y. Wang, *J. Am. Chem. Soc.*, 2015, **137**, 2688-2694.
49. A. Han, H. L. Chen, Z. J. Sun, J. Xu and P. W. Du, *Chem. Commun.*, 2015, **51**, 11626-11629.
50. Wang, X. G. Li, D. H. Xiong and L. F. Liu, *J. Mater. Chem. A*, 2016, **4**, 5639-5646.
51. C. G. Read, J. F. Callejas, C. F. Holder and R. E. Schaak, *ACS Appl. Mater. Interfaces*, 2016, **8**, 12798-12803.
52. X. D. Yan, K. X. Li, L. Lyu, F. Song, J. He, D. Niu, L. Liu, X. Hu and X. Chen, *ACS Appl. Mater. Interfaces*, 2016, **8**, 3208-3214.
53. G. F. Chen, T. Y. Ma, Z. Q. Liu, N. Li, Y. Z. Su, K. Davey and S. Z. Qiao, *Adv. Funct. Mater.*, 2016, **26**, 3314-3323.
54. X. L. Zhu, C. Tang, H. F. Wang, B. Q. Li, Q. Zhang, C. Li, C. Yang and F. Wei, *J. Mater. Chem., A* 2016, **4**, 7245-7250.
55. L. G. Feng, H. Vrabel, M. Bensimon and X. L. Hu, *Phys. Chem. Chem. Phys.*, 2014, **16**, 5917-5921.
56. M. Ledendecker, S. K. Calderín, C. Papp, H. P. Steinrück, M. Antonietti and M. Shalom, *Angew. Chem. Int. Ed.*, 2015, **54**, 12361-12365.
57. D. N. Liu, Q. Lu, Y. L. Luo, X. P. Sun, and A. M. Asiri, *Nanoscale*, 2015, **7** 15122-15126.
58. X. D. Jia, Y. Zhao, G. Chen, L. Shang, R. Shi, X. Kang, G. I. N. Waterhouse, L. Z. Wu, C. H. Tung and T. Zhang, *Adv. Energy Mater.*, 2016, **6**, 1502585.
59. Y. H. Liang, Q. Liu, Y. Luo, X. Sun, Y. He and A. M. Asiri, *Electrochim. Acta*, 2016, **190**, 360-364.

60. W. Z. Fang, D. Liu, Q. Lu, X. Sun and A. M. Asiri, *Electrochem. Commun.*, 2016, **63**, 60-64.